This is the Submitted Version of a Manuscript published in MRS Bulletin, DOI: 10.1557/s43577-024-00830-6

Exploring Electronic Band Structure and Surface Properties in SnO_2 Nanostructures with Enhanced Photocatalytic Activity

Mariangela Giancaspro[1,2], Marica Tancredi[1], Rosa Pia Di Fonzo[1], Pierluigi Lasala[1,2], Antonella Milella[1,3], Giuseppe Valerio Bianco[3], Teresa Sibillano[4], Cinzia Giannini[4], Rachele Castaldo[5], Gennaro Gentile[5], Massimo Delledera[2†], Carlo Nazareno Dibenedetto[2], Ilaria De Pasquale[2], Roberto Comparelli[2], Annamaria Panniello[2], Antonino Madonia[2‡], Marinella Striccoli[2,6], Maria Lucia Curri[1,2,6,*], Elisabetta Fanizza[1,2,6,*]

[1] *Chemistry Department, University of Bari, via Orabona 4 70126 Bari, Italy*
[2] *CNR-Institute for chemical physical process (IPCF), via Orabona 4 70126 Bari, Italy*
[3] *CNR-Institute of Nanotechnology (Nanotec), Bari Division, via Orabona 4, 70125 Bari, Italy*
[4] *CNR-Institute of Crystallography (IC), via Amendola 122/O, Bari 70126, Italy*
[5] *CNR-Institute of Polymers, Composites and Biomaterials (IPCB), Via Campi Flegrei 34, 80078 Pozzuoli (Naples) Italy*
[6] *National Interuniversity Consortium of Materials Science and Technology, INSTM, Bari Research Unit, 70126, Bari, Italy*

Corresponding authors: elisabetta.fanizza@uniba.it; marialucia.curri@uniba.it

Present address: †Chemistry Department, University of Milan, Via Golgi- 19, Corpo A, 20133 Milano, Italy ; ‡ Department of Physics and Chemistry "E. Segrè", University of Palermo, Palermo 90123, Italy

keywords: tin dioxide, oxide nanostructures, photocatalytic decolouration, photocatalysts physical-chemical properties

Abstract. Recent studies have explored SnO_2 nanostructures as photo/electro catalysts substitutes for TiO_2 in environmental remediation and energy-applications, due to this material sustainability and promising photo/electro-catalytic properties. This surge in interest is driving research endeavors aimed at unravelling the intricacies of the structure-function relationship, which remains not yet fully understood. Here, we present original insights into the precise control of SnO_2 nanostructures morphology, shaping nanoparticles into either spherical or rod-like form, through established and low-cost synthetic hydrothermal and precipitation methods. Employing a multidisciplinary approach encompassing structural, textural, chemical, and optical characterization tools, we carefully investigate the synthesized SnO_2 nanostructures, unveiling

and comparing their distinctive physical-chemical properties. Our comprehensive analysis reveals the complex relationship between specific synthesis methodologies, nanoparticles morphology, band gap structure and defects states, and surface characteristics. To substantiate these findings, we assess the photocatalytic activity of the synthesized materials in the decolorization of methylene blue (MB) dye as a model compound, using commercial TiO_2 P25 as a reference. The results confirm that manipulation of factors including morphologies, electronic and surface properties can be purposely exploited to improve the (photo)catalytic performance of the material.

1. Introduction.

In recent years, metal oxide nanoparticles (NPs) have garnered significant attention owing to their attracting chemical and physical properties, spanning optical, electrical, and photochemical characteristics, that hold great potential across a wide range of diverse applications.[1-2] Nanoscale metal oxides such as ZnO, TiO_2, SnO_2, CuO, In_2O_3, V_2O_5, and WO_3 have been extensively investigated and integrated into various cutting-edge technologies,[3-4] including solar cells,[5] lithium-ion batteries,[6] heterogeneous photocatalysis,[7] and biomedical applications.[8] SnO_2 has successfully sparked the researchers' interests due to its long-term stability, high oxidation potential, chemical inertness, corrosion resistance, non-toxicity, economic efficiency, and environmental protection.[3] Since 1976,[9] hundreds of research studies have investigated the photocatalytic activity of SnO_2 nanostructures in the advanced oxidation processes for the degradation of dyes, [10-12] and recalcitrant contaminants which pose environmental concern.[13] Recently, leveraging SnO_2 nanostructures for photocatalytic processes has emerged as a promising approach for generating value-added compounds from CO_2 [14] and for H_2 generation through water splitting,[15] all strategies able to contribute to mitigating energy shortages and environmental pollution. Regardless of the specific photocatalytic applications, numerous studies have focused on exploring effective approaches to overcome the inherent limitations of this material. They include its wide bandgap, which restricts absorption to ultraviolet light, thus underutilizing solar irradiation, and the recombination of photogenerated electrons and holes,[13] that hamper their exploitation in redox processes.

A complex balance among several factors such as efficient excitation, effective charge carrier separation and transfer at the interface, suitable valence band and conduction band edge potentials and density of defect states plays pivotal role towards enhancement of the photocatalytic

performance.[12] It can also be significantly increased through adsorption, which often serves as the initial stage in chemical transformations. Adsorption efficiency depends on specific photocatalyst surface area, surface charge and defects,[16] besides structure of the adsorbing molecule.[17-18] Therefore, engineering electronic band gap structure and surface properties has represented a convenient approach to enhance the photocatalytic activity.[19-21]

Colloidal syntheses, including a variety of solution-phase strategies have been employed to prepare SnO_2 NPs,[22-23] such as sol-gel synthesis,[24] reflux,[25] precipitation,[26] hydrothermal, solvothermal, microwave synthesis. [22, 27-29] They can control by a variety of parameters, such as pH and precursor concentration, the NP geometry [30] and their electronic features, tuning band gap via size, morphology and composition modulation as well as surface properties. Rod-shaped NPs are expected to show higher specific surface area and enhanced photophysical and photochemical properties; NPs in quantum confinement regime present enlarged band gap with respect to bulk counterpart; extrinsic doping in syntheses,[31] even at low weight percentage <10%, can induce band gap narrowing via mid gap defect states. Defects states can also act as trap sites, which can effectively improve the carrier separation,[9, 32] without affecting charge carrier transfer at the interface. Moreover, in semiconductor, defect sites usually act as effective active centres, which mainly accelerate the surface reactions.[21] Self-doping, occurring when Sn^{2+} is generated within the SnO_2, also induces band gap narrowing due to non-stoichiometric SnO_{2-x} structures arising from surface oxygen vacancies (V_O). Similarly, the occurrence of mesophase, like Sn_3O_4, red-shifts the absorption due to the narrowing of the band gap.

In addition to these core considerations, to accurately evaluate the suitability of a material for use as a photocatalyst, it is essential to investigate not only the efficiency in photocatalytic transformation but also, in line with the goals of energy conservation and environmental sustainability, attention should be directed towards assessing pollution levels, environmental impact, and production costs associated with the actual manufacturing process of the photocatalyst as well as its potential for reusability.[9, 17]

This study addresses some of the highlighted aspects, by developing colloidal syntheses of SnO_2 nanostructures via both hydrothermal and precipitation methods, which are easy and straightforward colloidal approaches, manipulating their morphology, surface and electronic proprieties tuning reaction conditions. Complementary optical, structural, and compositional characterizations, carried out on several samples, allow to unveil the experimental condition

providing, for each synthetic approach, either nanorods or nanospheres, without using additives or stabilizing agents, and the mechanism underpinning shape modulation is proposed. To highlight the strong interplay between structure-properties-function, the synthesized nanostructures are tested as photocatalyst in the decolouration process, encompassing both adsorption and UV-activated photocatalysis, using Methylene Blue (MB) as the model compound, with commercial TiO_2 P25 serving as reference. The physical-chemical properties of NPs, heavily influenced by distinct synthetic methods, significantly impact the photocatalytic process. This results in SnO_2 NP samples synthesized under well-defined reaction conditions demonstrating superior efficiency in the decolouration process compared to TiO_2 P25 and distinct photophysical properties affecting their photocatalytic behaviour. Rod-like nanostructures, synthesized by precipitation method, promote the complete decolouration of MB via an adsorption-driven pathway thanks to surface properties, including high specific surface area (SSA) and surface charge density. In the case of spherical, quantum confined NPs, synthesized by hydrothermal approach, the generation of reactive oxygen species (ROS), thanks to the proper match of the band edge potential with the $H_2O/OH\cdot$ and $O_2/\cdot O_2^-$ couples redox potential, promotes MB oxidation. Finally, recovery and recyclability tests on the best performing catalysts are performed.

2. Materials and Methods.

For the synthesis of the SnO_2 nanostructures and photocatalytic experiments the following materials $SnCl_4\cdot 5H_2O$ (98%), sodium hydroxide (NaOH), Methylene Blue (MB), 2-hydroxy terephthalic acid (hTPA, 97%), terephthalic acid (TPA, 98%) were purchased from Sigma-Aldrich. Absolute ethanol and deionized or milliQ water (18 Ω) were used without further purification.

Synthesis of SnO_2 nanostructures by hydrothermal method (SnO_h). The tin precursor solution was prepared by dissolving $SnCl_4\cdot 5H_2O$ (0.09 M) in a H_2O and ethanol (EtOH) mixture 1:3 (volume ratio) and by adjusting the pH at 6 or 12 adding NaOH. The rapid precipitation of hydroxides or hydrochloride species made the reaction mixtures turbid, turning it into a white slurry. Then it was transferred to a Teflon-lined stainless autoclave (15 mL) and kept at 180 °C for 6 h at ~10 bar under continuous stirring. The suspension was finally collected by centrifugation at 15 000 x g (Technical centrifuge mod. Centric 322A) and washed with a 1:1 EtOH: H_2O (DI) mixture. Two cycles of re-dispersion/centrifugation were carried out, followed by placing the

recovered pellet in an oven at 60°C overnight and manually grinding it to achieve a fine powder. The sample synthesized at pH 6 was labelled SnO_h1 and that at pH 12, SnO_h2.

Synthesis of SnO_2 nanostructures by precipitation method (SnO_p). For the sol-precipitation synthesis, the $SnCl_4 \cdot 5H_2O$ solution (0.09 M) tweaked at pH 10 by NaOH was let to react at room temperature for 10 minutes and then poured in a closed vial and placed into a silicon oil bath. Two methods were employed to heat the samples: a rapid heating ramp at nearly 2°C per minute from room temperature (25°C) to 80°C (SnO_p1), and immersion of the vial into a pre-heated oil bath at 80°C (SnO_p2). Following heating, the suspensions were stirred for 6 hours, resulting in the formation of either a milky or deeply grey slurry, depending on the method used. Purification was carried out by centrifugation at 15000 x g followed by successive addition of 1:1 EtOH:H_2O deionized mixture and centrifugation. The recovered powder was dried in an oven at 60°C overnight and manually grinded to obtain a fine powder.

Photocatalytic experiments. The photocatalytic activity of the SnO_2 nanostructures was evaluated according to the ISO 10678:2010 standard. 5 mg/mL of the NP powder was suspended into 100 mL of MB 10^{-5} M aqueous solution adjusting the pH to 6 by addition of NaOH and/or HCl. Experiments were also carried out setting the pH at 10. Following an initial stirring period in the absence of light, the suspension was transferred to an open flask and positioned 10 cm away from an Hg-UV lamp emitting light at λ=254 nm with an intensity of 0.2 mW/cm^2. Throughout UV-light exposure, samples of the suspension were periodically withdrawn at specified intervals, centrifuged, and the UV-Vis absorption spectra of the resulting supernatant were measured. The absorbance intensity at 664 nm, maximum wavelength of the MB absorption band, was used to determine the concentration by Lambert-Beer law, using the extinction coefficient value of 8.4 10^4 L mol^{-1} cm^{-1}. Percentage of decolouration was calculated from the following equation:

$$\%Decolouration = \left(\frac{A_0 - A_t}{A_0}\right) \times 100$$

where A_0 is the initial absorbance of the solution and A_t is the absorbance value at each selected time. For recycling experiment, freshly prepared MB solution at the 10^{-5}M concentration was added to SnO_2 powder collected from previously performed photocatalytic test by centrifugation, dried in an oven at 60°C.

Detection of photogenerated OH radicals. Photoluminescence spectra of hTPA stock solutions in the range of 0.01-1 μM in NaOH $2 \cdot 10^{-3}$ M, were recorded (λ_{ex} = 310 nm) from 330 nm-600 nm, and a calibration curve was traced by plotting the integrated emission band versus concentration of hTPA stock solutions (slope= $8.1 \cdot 10^{6}$ μM^{-1}). This calibration curve can provide the quantitative determination of ·OH released *in situ* during the photocatalytic experiment, probed by TPA. For this purpose, TPA solution with a concentration of $5 \cdot 10^{-6}$ M was prepared in aqueous solution of NaOH $2 \cdot 10^{-3}$ M. 5 mg/mL of SnO_2 nanostructures were added to 10 mL of this solution, and the suspension was irradiated using the same set up exploited for the photocatalytic experiments. Blank experiment carried out without addiction of the photocatalyst to the TPA solution was also performed. Each suspension/solution was irradiated for 60 minutes, the supernatant was recovered by centrifugation, and the photoluminescence spectrum was recorded. Based on the calibration curve, the concentration of ·OH was calculated by integrating the emission band.

Characterization techniques.

UV-Vis absorption were recorded using a Cary 5000 (Varian) UV/Vis/NIR spectrophotometer, equipped with an integration sphere to acquire diffuse reflectance spectra. The optical band gap, E_{gap}, value was obtained from diffuse reflectance spectra by Kubelka-Munk model and Tauc's plot according to the following equation:

$$(F(R)\,h\upsilon)^{1/n} = \beta\left(h\upsilon - E_{gap}\right)$$

where F(R) is the Kubelka-Munk function, E_{gap}, hν and β represent the optical band gap, photon energy and a costant respectively, and n value is ½ for SnO_2 allowed direct transition. The estimation of the E_{gap} was conducted by identifying and analyzing the linear part of the Tauc plot extrapolated to the x-axis.

Photoluminescence (PL) spectra were acquired by a Fluorolog 3 spectrofluorimeter (HORIBA Jobin-Yvon), equipped with a 450 W xenon lamp as exciting source and double grating excitation and emission monochromators All the measurements were performed at room temperature. The PL emission was detected by a picosecond photon counter (TBX ps Photon Detection Module, HORIBA Jobin-Yvon). Excitation wavelength in the range from 280 to 400 nm were tested for SnO_2-based drop-casted films on quarts and the most suitable excitation wavelength (310 nm) was selected.

TEM measurements were performed on a JEOL JEM1011 electronic microscope operating at 100 kV, equipped with a high-resolution CCD camera, using a tungsten electron source. The

sample powders were dispersed in ethanol, and the suspensions were sonicated for 1 hour to achieve a uniform dispersion. 3 µl of the diluted suspension in EtOH were drop-casted on a 400 mesh amorphous carbon-coated Cu grid, letting the solvent evaporate.

For ζ- potential measurement, a Zetasizer nano ZSP (Malvern, Worcestershire, United Kingdom) equipped with a laser diode that works at 50 mW and at a wavelength of 532 nm, was used. For the analysis, a solution of 7 µg/mL in filtered ultrapure water was used.

Nitrogen adsorption analysis was performed to evaluate the textural properties of the SnO_2 nanostructures. Brunauer-Emmett-Teller (BET) specific surface area was evaluated by N_2 adsorption at 77 K through a 3Flex analyzer (Micromeritics, Norcross, GA, USA). Total pore volume of the samples was measured at 0.995 p/p^0 and pore size distribution was evaluated through the Non-Local Density Functional Theory (NLDFT) model. The adsorption measurements were performed using high purity gases (>99.999%). The samples were degassed for 10 h at 150 °C under vacuum before analysis ($P < 10^{-7}$ mbar). Interparticle pore volume was evaluated at 0.995 p/p^0.

The FTIR characterization was carried out using a Varian 670 FTIR spectrometer equipped with a diamond attenuated total reflection (ATR) accessory of 2 mm and a deuterated tryglicine sulfate detector. 1 µl of each sample was put on the internal reflection element and then the spectrum was recorded in the range 4000-400 cm^{-1} using 16 accumulation scans acquired with a nominal resolution of 1 cm^{-1}.

Raman spectra were collected by using a LabRAM HR Horiba spectrometer with a 532 nm continuous excitation laser source. Measurements were carried out under ambient conditions at a low laser power (1 mW) to avoid laser-induced damage of the sample. The Raman signal from the silicon wafer at 520 cm^{-1} was used to calibrate the spectrometer, and the accuracy of the spectral measurement was estimated to be 1 cm^{-1}.

X- Ray diffraction (XRD) patterns of powders were collected by a Rigaku RINT2500 rotating anode diffractometer (50 kV, 200 mA) equipped with a silicon strip Rigaku D/teX Ultra detector. An asymmetric Johansson Ge(111) crystal was used to select the monochromatic Cu Kα1 radiation (λ= 1.54056 Å). Measurements were executed in transmission mode by introducing the sample powder in a Lindemann capillary tube with a diameter of 0.5 mm. The XRD patterns were recorded in the range of 2θ = 10−100° by step scanning, using 2θ increments of 0.02° and a fixed counting

time of 2s/step. A qualitative analysis of the crystalline phase content was performed using the QUALX 2.0 program.

X-ray photoelectron spectroscopy (XPS) analyses were performed with a Scanning XPS Microprobe (PHI 5000 Versa Probe II, Physical Electronics) equipped with a monochromatic Al Kα X-ray source (1486.6 eV), operated at 15 kV and 24.8 W, with a spot of 100 μm. Survey (0–1200 eV) and high- resolution spectra (Sn3d, O1s) were recorded in Fixed Analyser Transmission (FAT) mode at a pass energy of 117.40 and 29.35 eV, respectively. A dual beam charge neutralization, with a flux of low energy electrons (∼1 eV) combined with very low energy positive Ar^+ ions (10 eV), was used to compensate for surface charging. The hydrocarbon component of the C1s spectrum, fixed at 284.8 eV, was used as the internal standard for charging correction. All spectra were collected at an angle of 45° with respect to the sample surface. ThermoFisher Scientific Database was used as extensive knowledge base of information regarding XPS analysis and the elements characterized.

3. Results and discussion

Morphological, optical, and structural characterization of as-synthesized SnO_2 nanostructures. SnO_2 nanostructures have been synthesized using either precipitation (samples labelled SnO_p) or hydrothermal (samples labelled SnO_h) approaches, with adjustment made to pH, heating condition and precursors concentration. The tin salt undergoes to alcoholises, with formation of a white precipitates, ascribed to $Sn(OH)_xCl_y$ or $Sn(OH)_4$, that upon dehydration and oxidation generate the SnO_2 NPs. To slow down the reaction kinetics and achieve improved morphological control, an excess of alcoholic solvent (ethanol) relative to water was chosen, specifically 3:1 volume ratio. Moreover, due to the inherent acidity of $SnCl_4$ precursor, NaOH has been always added to the reaction mixtures to set the proper pH. Indeed, a large excess of NaOH has been requested to raise the pH of the reaction mixture for those syntheses carried out under alkaline condition. For each synthetic method, reaction conditions have been optimized to provide high yield of either rod-shaped or spherical NPs, as reported in the table in Figure 1, opening the venue to investigate the role played by morphology in the photocatalytic behaviour.

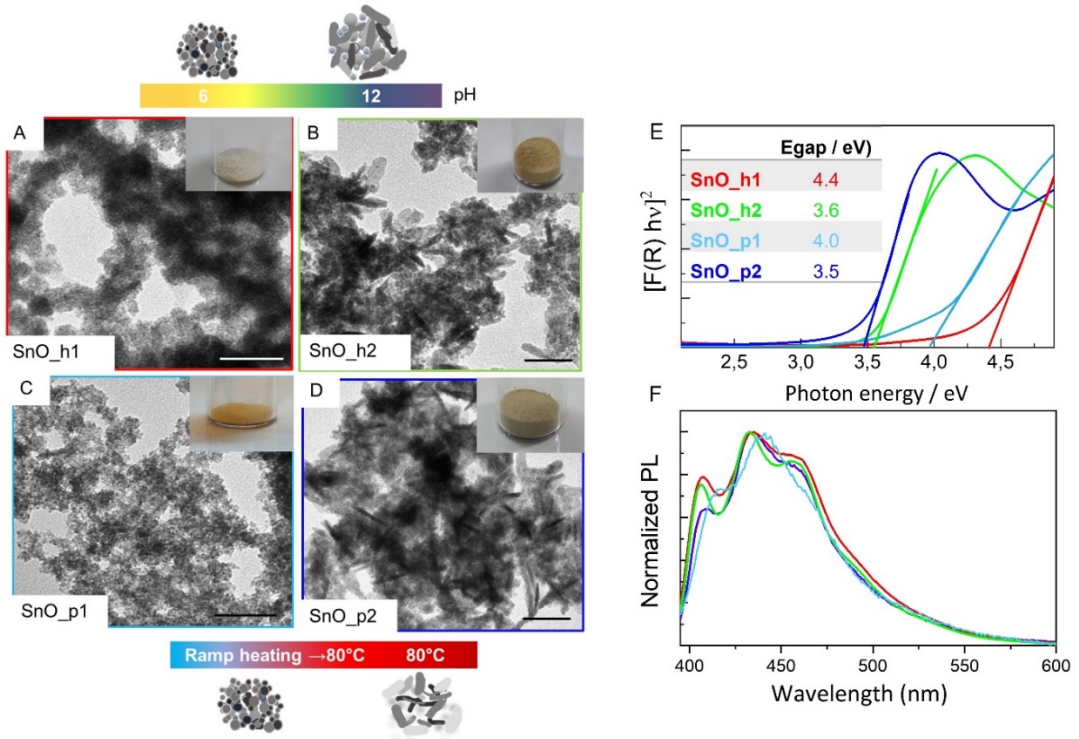

G

Synthetic method	Synthetic Condition	Nanostructure Shape
SnO_h1	Hydrothermal	pH 6	Spherical
SnO_h2	Hydrothermal	pH 12	Rod-like
SnO_p1	Precipitation	pH 10 – heating ramp from RT to 80°C	Spherical
SnO_p2	Precipitation	pH 10 – 80°C	Rod-like

Figure 1. (A-D) TEM micrographs (scale bar 50 nm) of SnO_2 nanostructures synthesized by hydrothermal (A, B, SnO_h1 and SnO_h2) or precipitation method (C, D, SnO_p1 and SnO_p2). In the inset: pictures of the obtained powders; (E) Tauc plot for energy gap (E_{gap}) determination obtained from diffuse reflectance spectra of SnO_2 samples, E_{gap} value reported as inset table; (F) Normalized photoluminescence (PL) spectra (λ_{ex}= 310 nm) of drop casted SnO_2 film. Colour code: SnO_h1: red, SnO_h2: green, SnO_p1: pale blue, SnO_p2 blue; (G) Table summarizing the synthetic approach and condition used for the synthesis of each selected samples and the shape, as shown by TEM characterization.

Rod-like geometry theoretically gives higher specific surface area than spherical NPs, and at the same time is expected to enhance spatial charge separation, thus leading to improved photocatalytic performance.[33] In Figure 1 the morphological characterization by TEM of SnO_2 NPs samples synthesized by hydrothermal, labelled SnO_h1, SnO_h2 and precipitation approach, labelled SnO_p1, SnO_p2 are reported. SnO_h1 and SnO_p1 mainly consist in nanospheres while SnO_h2 and SnO_p2 in nanorods. In the hydrothermal approach, raising the pH of the reaction mixture from 6 to 12 has induced a transition in NP shape from predominantly spherical, with 1-2 nm-sized diameter (SnO_h1, synthesized at pH 6) to mainly rod-like nanostructures (SnO_h2,

obtained at pH 12). It is well known [34] that Na^+ ions selectively adsorb to specific crystallographic face. Therefore, the formation of rod-like NPs under alkaline pH conditions set by NaOH, can be attributed to a facet control growth induced by large excess of Na^+ cations.[34]

In contrast to the hydrothermal approach, which facilitates the formation of SnO_2 NPs even under nearly neutral pH conditions due to high pressure and temperature, the precipitation method necessitates alkaline pH levels to initiate nanoparticle formation. Maintaining the reaction mixture at pH=10, spherical NPs with an average diameter of 1-2 nm are attained through a gradual heating process (sample SnO_p1) using a heating ramp transitioning from room temperature to 80°C, while anisotropic nanostructures are achieved (sample SnO_p2) by immersing the flask containing the reaction mixture in a preheated oil bath at 80°C.

It can be reasonably inferred that during gradual heating of the solution, hydrolysed monomers are released slowly, facilitating the isotropic growth and the formation of small spherical NPs. Conversely, a sudden increase in the temperature of the reaction mixture temperature leads to a high nucleation rate followed by an oriented attachment mechanism assisted by the presence of NaOH, which allows the growth of nanorods. Optical band gap, E_{gap} values have been determined by transforming diffuse reflectance spectra from drop-casted film by Kubelka−Munk analysis using the Tauc method [35] (Figure 1E). The E_{gap} values estimated for SnO_h1 and SnO_p1, 4.4 eV and 4.0 eV, respectively, greater than that of bulk SnO_2 (3.6 eV), confirm that NPs are in quantum confinement regime, as supposed from size statistical analysis by TEM, pointing out an average NP radius below SnO_2 exciton Bohr radius (2.7 nm). Conversely, E_{gap} values close to SnO_2 bulk value have been calculated for SnO_h2 and SnO_p2 (3.6 eV and 3.5 eV, respectively).

Fluorescence spectra have been performed exciting the samples at 310 nm (Figure 1F). In metal oxide, fluorescence mainly arises from radiative recombination from mid-gap or shallow defect states, mainly V_O. The emission spectrum of nanosized SnO_2 are generally broad bands in the UV-visible range with emission involving energy level arising from surface or bulk defects states.[36-37] Similarly, the broad emission spectra observed in drop casted film (Figure 1F) show a structured profile covering the blue region of the electromagnetic spectrum along with a tail expanding up to 600 nm.[36-37] The peaks around 410 nm, corresponds to electron transitions from near the conduction band edge to the valence band edge mediated by V_O, and others at higher wavelength (nearly 440 nm) may correspond to a luminescence centre formed by tin interstitial or dangling bonds present in the materials. Broadening of the PL band can be ascribed to the degeneracy

expansion of defect levels below the conduction band edge that are produced because of V_O. Emission at wavelengths > 510 nm can be originated from recombination from mid-gap states to valence band edge. Despite slight variations, all samples exhibit similar emission band profiles, although a minor red-shift in the fluorescence spectrum is noted in SnO_p1.

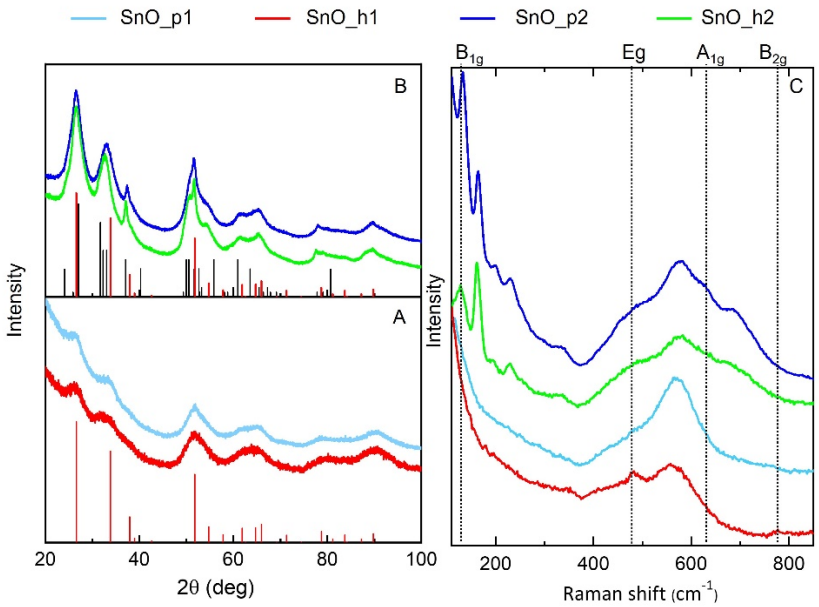

Figure 2. (A, B) X-ray diffraction pattern, (C) Raman spectra of SnO_h1 red trace, SnO_h2 green trace, SnO_p1 pale blue trace, SnO_p2 blue trace. In panel A and B reference pattern of SnO_2 (red bar JCPDS card No. 00-071-0652) and Sn_3O_4 (black bar, JCPDS card No. 16-0737) are reported.

Structural and chemical characterization have been also carried out. X-ray diffraction patterns (Figure 2) of SnO_h1 and SnO_p1, show broader peaks as expected from nanosized particles, with an XRD pattern well- fitting the tetragonal structure of cassiterite SnO_2 (red bar in Figure 2A and 2B, JCPDS card No. 00-071-0652). Conversely, narrower diffractions peaks are displayed by SnO_h2 and SnO_p2, confirming the presence of larger nanostructures. Additional peaks at 2θ= 37°, two overlapped peaks at around 2θ= 50° and one at around 2θ= 77.5° are identified as an additional phase of Sn_3O_4 (black bar in Figure 2B JCPDS card No. 16-0737) by a qualitative phase analysis. Therefore, these samples show the presence of a mixture of phases composed by a main phase of cassiterite SnO_2 and minor phase of Sn_3O_4. Raman analysis (Figure 2C), conducted in conjunction with XRD, has been utilized to enhance the structural and chemical characterization of the material.[38]

It is worth noting that bulk SnO_2 with a tetragonal rutile structure typically presents four main active Raman peaks: B_{1g} at 123cm^{-1}, E_g at 473 cm^{-1}, A_{1g} at 634 cm^{-1}, and B_{2g} at 773 cm^{-1}. [35] For

SnO_2 particle with size < 15 nm, as in the case of SnO_h1 and SnO_p1, Raman spectra of SnO_2 NPs turns into a broad feature between 400 and 700 cm^{-1} with a maximum around 570 cm^{-1} due to the appearance of the D peak. Several studies attribute the origin of this theoretically forbidden Raman mode to surface V_O and, specifically, to the presence of a non-stochiometric shell around SnO_2 NPs.[35, 39] The appearance of D peak results on the reduction in the contribution of the four Raman active modes of SnO_2 which became less and less evident as particle size decreases. E_g and B_{2g} peaks are also distinguished in the spectrum of SnO_h1 sample (Figure 2C red trace), confirming that SnO_2 NPs have a crystalline core with tetragonal rutile structure. However, they become less evident and almost disappear in SnO_p1 sample probably due to the smaller average size of NPs in this sample.[22]

Spectra of samples SnO_h2 and SnO_p2, both rod-like nanostructures, also presents a broad feature between 400 and 750 cm^{-1} dominated by the D peak at 570 cm^{-1}. In these samples, B_{1g} is clearly visible while E_g, A_{1g} modes, together with the (A_{2u})V(LO) mode around 690 cm^{-1} can be distinguished as shoulder in the spectra. Moreover, the spectra show distinct Raman peaks at lower wavenumbers (between 150 and 250 cm^{-1}) that can be associated to transition oxide phases [40] as well as to elastic vibrations of the SnO_2 nanorods itself, that is the confined acoustic phonon modes in a nanorod, according to previous Raman studies.[41]

Therefore, the results of the structural characterization and the emission analysis allow to infer that SnO_2 nanostructures show defects states, mainly V_O related and the presence of a non-stochiometric shell around SnO_2 NPs for SnO_h1 and SnO_p1 and of transition oxide phases for SnO_h2 and SnO_p2.

X-ray photoelectron spectra (XPS) have been also recorded to identify the chemical states of the SnO_2 samples. High-resolution XPS spectra of Sn3d and O1s are presented in Figure S1a and Figure 3, respectively. The $Sn3d_{5/2}$ spectrum reveals a binding energy of 487.2 eV, indicating Sn^{+4}, with no appreciable signals ascribed to Sn at different oxidation state being detected.[42] The lineshapes of Valence Band spectra (Figure S2) are also characteristic of Sn^{+4} oxidation state.

High resolution spectrum of O1s (Figure 3) for each investigated sample displays a broad band, that can be best fitted with three components: the one at nearly 530.8 eV originates from the O^{2-} state in SnO_2, while those at higher binding energy, at nearly 533 eV, are assigned to chemisorbed oxygen atoms, hydroxyl groups and organic oxygen. However, the contribution due to Sn-OH results more intense than that corresponding to oxygen in the SnO_2 network in SnO_h2, suggesting

differences in chemical states with respect to SnO_h1, SnO_p1 and SnO_p2 samples. Indeed, FT-IR spectrum recorded in ATR mode of SnO_h2 (Figure S3) is dominated by a broad and intense absorption band at 1017 cm^{-1} attributed to Sn-O stretching of tin oxyhydroxide species.[43] The profile of the high-resolution spectra of the O1s of the SnO_p1 together with a prominent Cl2p signal (Figure S1b), corresponding to inorganic chloride, suggest the presence, in this sample, of tin oxychloride species.

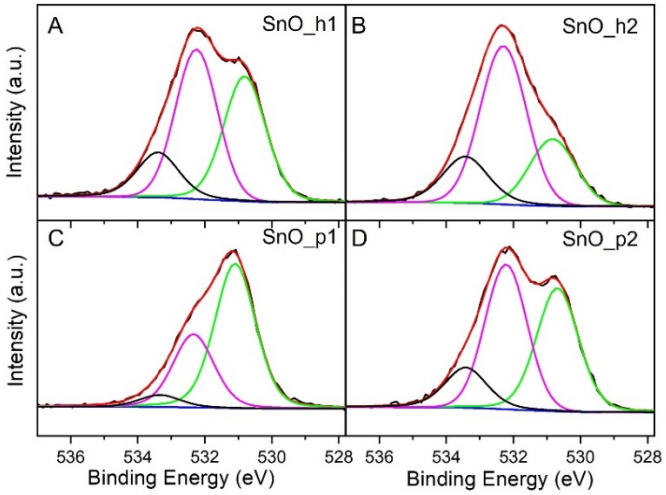

Figure 3. High resolution spectrum of O1s for SnO_h1 (A), SnO_h2 (B), SnO_p1 (C), SnO_p2 (D).

The quantitative analysis carried out by integrating the O1s peak component associated with the oxygen bound to tin and that of the Sn3d, allows to estimate the O/Sn ratio. This ratio, which is < 2 for SnO_h2, SnO_p1 and SnO_p2, supports the notion of non-stoichiometric SnO_2 phase, while an almost stoichiometric O/Sn ratio has been estimated for SnO_h1.

Nitrogen adsorption/desorption isotherms (Figure 4A) have been recorded for all the samples and specific surface area (SSA), total pore volume (V_{tot}) and pore size distribution (Figure 4B) have been evaluated. ζ-potential measurements (Figure 4C) have been also performed for the SnO_2 nanostructures dispersions to estimate the isoelectric point. In heterogeneous catalysis, the porosity and the surface charge of photocatalysts play a crucial role in determining the adsorption yield of molecules. This adsorption, whether due to physisorption or chemical affinity, may serve as a preliminary step before chemical transformation occurs. The rod-like nanoparticles (SnO_p2 and SnO_h2) and the spherical nanoparticles SnO_h1 show nitrogen adsorption isotherms indicating the presence of large mesopores and macropores (from 4-5 nm to about 100 nm) and a very limited amount of microporosity, as shown by pore size distribution graphs (Figure 4B), that account for

a total pore volume of 0.78, 0.76 and 0.67 cm^3/g, respectively. On the other hand, SnO_p1 exhibit very small nitrogen adsorption on all the pressure range, displaying indeed very low amount of porosity (0.06 cm^3/g) of width up to 4 nm.

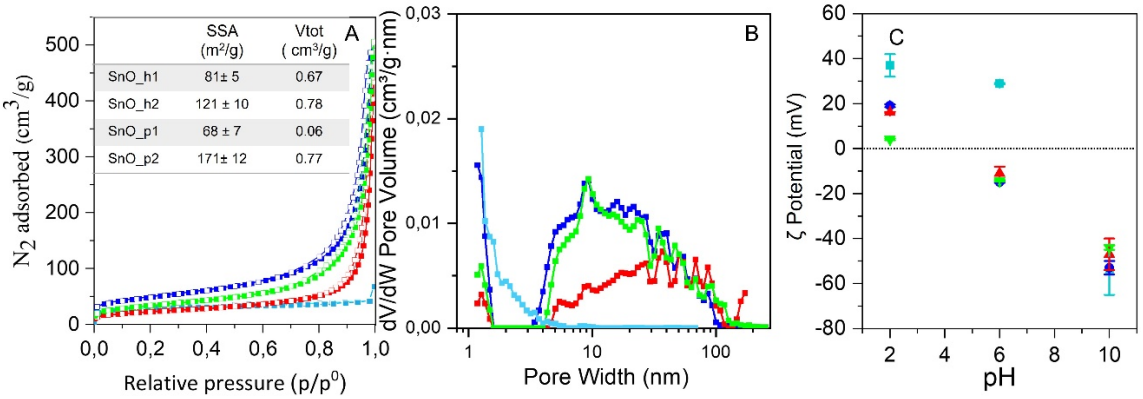

Figure 4. (A) Nitrogen adsorption/desorption isotherm of all the as-synthesized SnO_2 samples and relative value of specific surface area (SSA) and pore total volume (Vtot), (B) NLDFT pore size distribution, (C) ζ-potential of all the samples diluted in filtered water adjusting the pH at 2, 6, 10 by HCl or NaOH. Colour code: SnO_h1 red, SnO_h2 green, SnO_p1 pale blue, SnO_p2 blue.

For all these particles, the porosity is to be ascribed to interparticle pore volume, which is therefore very limited in sample SnO_p1. SSA values reflect the pore size distributions trends, with SnO_p2, for which the micropores contribution is the largest, exhibiting the highest SSA value (171 m^2/g), SnO_h2 and SnO_h1 exhibiting respectively 121 and 81 m^2/g and SnO_p1 showing the lowest value of SSA of 68 m^2/g.

ζ-potential value of each sample has been measured in aqueous media at different pH, namely pH=2, nearly neutral pH (pH=6), and pH=10 (Figure 4C). SnO_p1 shows a positive ζ- potential value both at pH 2 and pH 6, and a negative value at pH=10, thus suggesting an isoelectric point at pH> 6. The ζ-potential values of SnO_h1, SnO_h2, and SnO_p2, positive at acidic pH, becomes negative at pH=6 and even more negative at pH=10, therefore an isoelectric point falling at pH< 6 would be expected for these samples.

Based on these preliminary surface characterizations, positively charge molecules can electrostatically interact with SnO_h1, SnO_h2, and SnO_p2, at pH=6, being their surface negatively charge. The adsorption step could be expected to be even more enhanced in SnO_h2 and SnO_p2 thanks to their high SSA values.

UV-activated heterogenous photocatalysis by SnO_2 nanostructures for the decolorization of Methylene Blue. Photocatalytic activity of the as-synthesized SnO_2 nanostructures have been

tested by suspending each SnO_2 sample (5 mg/mL) into aqueous solution of MB (10^{-5} M at pH=6) [44], a cationic dye chosen as target compound (Figure 5A). Several reports investigated the photocatalytic degradation [45-47] of MB using different class of photocatalysts. The great attention dedicated to this dye derives from its wide field of applications (textile, pharmaceutical, paper, dyeing, printing and food industries) as well as from its high thermal and light stability, that, combined with toxicity and non-biodegradability, makes its presence in wastewater an environmental concern.[48] The high molar absorptivity of MB ensures a striking and easily monitored decolouration of MB solution in water, which can be easily followed by absorption spectroscopy by monitoring the bleaching of the absorption feature at 664 nm associated to MB monomer.[49]

Here, first, adsorption under dark of the dye on each photocatalyst has been investigated and then UV-light induced photocatalytic experiments have been carried out. Both steps, adsorption and photocatalysis, have been monitored by recording the absorption spectra of supernatants recovered from the suspensions by centrifugation. In Figure 5 the set up and the results of the MB bleaching under dark and upon UV irradiation in the presence of each SnO_2 nanostructure are reported and compared to that achieved using TiO_2 P25 as reference photocatalyst (Figure 5C black line and symbols), and by monitoring the MB photolysis process (Figure 5C dark yellow line and symbols), as blank experiments. An adsorption time of thirty minutes has been demonstrated sufficient to reach the equilibrium condition. Figure S4 reports the absorption spectrum of the supernatant after adsorption and bar graphs displaying the value of the equilibrium amount (mg) of dye adsorbed per grams of photocatalysts (Q_e). It is worth noting that the absorption spectra of the MB still retain the same profile while decreasing in intensity, suggesting that no appreciable changes in the MB structure occur under dark. Conversely, under UV-light irradiation, bleaching of the absorption profile is generally accompanied by a slight blue-shift of the absorption feature of MB at 664 nm, with the overall spectrum decreasing in intensity as shown in Figure S5. Upon UV irradiation, the photocatalytic degradation of MB is anticipated to produce new species in the solution, characterized by a reduced degree of conjugation.

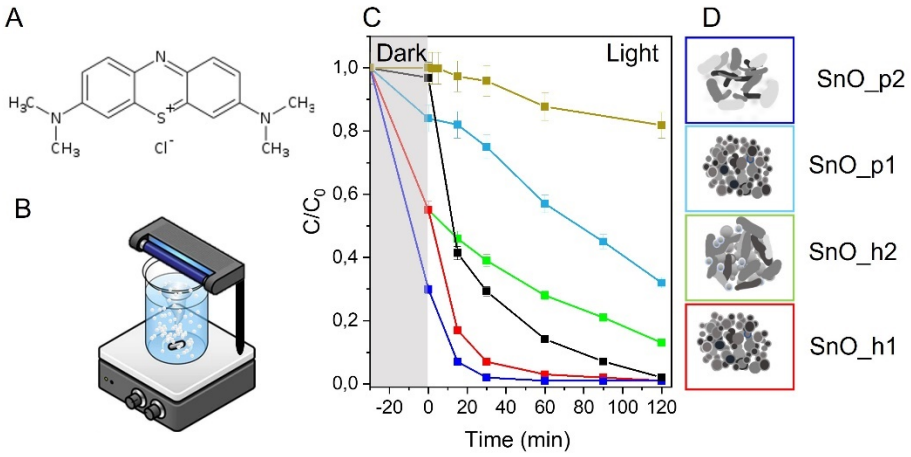

Figure 5. (A) Methylene Blue (MB) molecular structure, (B) set-up of the UV-light activated photocatalytic experiment, (C) MB decolouration under dark and upon UV light irradiation of each SnO_2 nanostructures, whose sketches are reported in panel D. The data are compared with those recorded for TiO_2 P25 (black lines and symbols) and photolysis of MB (yellow line and symbol), respectively, plotted in panel C.

The C/C_0 values calculated for adsorption/photocatalytic experiments carried out with each photocatalyst are reported in Figure 5C. Significant adsorption of MB on SnO_h1, SnO_h2, and SnO_p2 has been observed, resulting in a decrease in dye concentration to nearly half of its initial value for SnO_h1 and SnO_h2, and to one-third for SnO_p2. The favourable surface characteristics, including porosity and a high density of negatively charged surface, as demonstrated in prior analyses, contribute to the significant adsorption capacity observed for these samples with MB. Despite SnO_p1 shows a SSA comparable to that of SnO_h1 and exhibits some microporosity, its very low pore volume and positive surface charge density at pH=6 contribute to the observed poor adsorption of MB by this photocatalyst. Similarly, TiO_2 P25, showing concomitant positive surface charge density (isoelectric point above pH=6) and poor textural properties (SSA value of nearly 60 m^2/g),[50-51] also displays poor MB adsorption. As shown in Figure S4, adsorption of MB by SnO_2 nanostructures is generally enhanced as the pH increases to 10, a point at which all the photocatalysts exhibit negative surface charge density. However, even though improved at this pH condition, the adsorption capacity of SnO_p1 remains lower than that of SnO_h1 (Figure S4). Indeed, the low V_{tot} measured for SnO_p1 still limits the diffusion of both solvent and dye from the solution towards its surface. Consequently, this limitation hampers the interaction of the dye with NP surface, primarily due to Van der Waals forces.

By irradiating the suspension with UV-light lamp, decolouration of the solution becomes prominent. After 30 minutes of irradiation, MB solution is almost completely bleached by SnO_p2 showing a percentage of decolouration of 97%, followed by SnO_h1 (91%)> TiO_2 P25 (72%)> SnO_h2 (60%)> SnO_p1 (22%). A complete decolouration is achieved by SnO_h1 after 60 minutes; TiO_2 P25 requires 120 minutes for complete MB bleaching, while MB decolouration percentage of nearly 89% and 71% are measured for SnO_h2 and SnO_p1 at 120 minutes of irradiation, respectively. It is worth noting that poor photolysis is observed when irradiating the MB solution without photocatalysts, underscoring the dye's significant stability under UV light.

To gain deeper insight into the distinct behaviour exhibited by the SnO_2 nanostructures tested in the decolouration of MB, control experiments have been performed aiming at assessing the role of ROS in the photocatalytic activity.

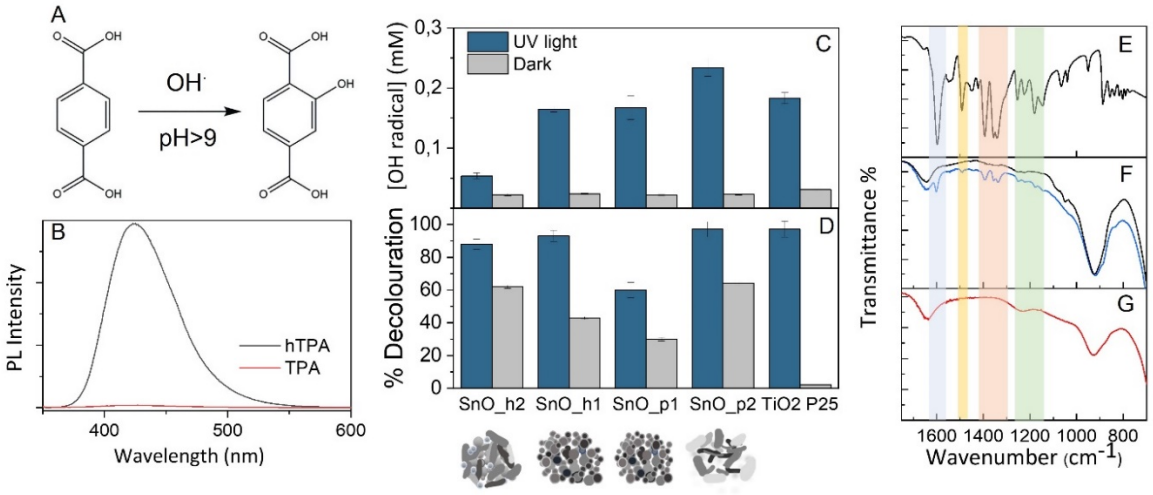

Figure 6. (A) Scheme of the reaction between terephthalic acid (TPA) and hydroxyl radical generating the fluorescent specie of 2-hydroxy terephthalate (hTPA); (B) fluorescence spectra of TPA and hTPA, (C-D) bar graph of (C) the concentration of hydroxyl radical (·OH), determined from fluorescent spectra and calibration curve with standard solution of hTPA and of (D) the percentage of decolouration of MB for each SnO_2 photocatalyst after 60 minutes of UV-irradiation (pH=10), (E-G) FTIR spectra in ATR mode of (E) Methylene Blue, (F) SnO_p2 sample before (black trace) and after MB adsorption under dark (blue trace), and (G) after 120 minutes of UV lamp irradiation

It is worth noting that the photocatalytic properties of materials rely on their ability to generate electron-hole pairs,[52] that, via surface charge transfer, can generate ROS [53] such as hydroxyl radicals (·OH) from photoexcited holes or superoxide radicals ($\cdot O_2^-$) from photoexcited electrons. This ROS can then trigger additional reactions leading to further generation of ·OH.[54] Recent studies have shown that the photoactivity of bulk SnO_2 nanostructures mainly arises from the ·OH

radical formation produced by oxidation of adsorbed water molecules (E^0 ·OH/H_2O = 1.97 V versus NHE at pH=7) or hydroxyl anions (E^0 ·OH/$^-$OH = 1.89 V versus NHE at pH 10) from photogenerated holes (E_{VB} = 3.8 V versus NHE).[55-56] Due to the more negative redox potential of O_2^- radicals for the O_2/·O_2^- (E^0 O_2/·O_2^- = -0.33 V versus NHE at pH=7) compared to the conduction band potential of bulk SnO_2 (E_{CB} = 0.2 V versus NHE),[57] it is not anticipated that these species will be generated by bulk SnO_2 upon UV photoexcitation. In literature, terephthalate (TPA) has been reported as a suitable probe to test the generation of ·OH. In basic aqueous medium it readily reacts with ·OH to produce strongly fluorescent compound hTPA (Figure 6A-B).Following the preliminary establishment of a calibration curve using standard hTPA solutions at various concentration (Figure S6A), the quantitative determination of ·OH, produced by the photocatalysts and probed by TPA, has been performed. Since the TPA acts as ·OH probe at alkaline pH, the results have been compared with the photocatalytic activity at the same pH condition (Figure S6) to elucidate the role of ·OH in the photocatalytic decolouration.

In Figure 6 the bar graph in panel C reports the estimated concentration of ·OH after 60 minutes of UV irradiation (blue bars) and under dark (grey bars) generated by each photocatalysts, while panel D displays the percentage of decolouration of MB at the same pH conditions. Poor generation of ·OH under dark have been detected for all the samples, while ·OH production increases upon UV-light irradiation, with values that strongly depend on the SnO_2 nanostructures used as photocatalyst. From the quantitative analysis, the following order of efficiency in the ·OH generation has been established SnO_p2> TiO_2 P25> SnO_h1> SnO_p1> SnO_h2. The low production of ·OH by SnO_h2 supports the incomplete decolourization promoted by this photocatalyst under UV irradiation (Figure 6D). Even though the percentage of decolouration reaches 86%, however, more than 60% can be ascribed to adsorption (grey bar displaying the decolouration under dark). Indeed, this powder sample, collected after the photocatalytic experiment, still retains the characteristic blue colour, indicative of the presence of adsorbed MB (data not shown). In contrast, both samples SnO_p1 and SnO_h1 displays notable production of ·OH. This greatly contributes to the photocatalytic discolouration performed by SnO_p1, featuring poor adsorption. Decolouration progresses from 29% and 43% under dark, to 59% and 93% upon UV-light exposure for SnO_p1 and SnO_h1, respectively. Similarly, decolouration induced by TiO_2 P25 can be expected to be highly promoted by the ·OH, largely generated by this photocatalyst, that shows almost negligible adsorption. A high concentration of ·OH as well as

high yield of MB adsorption could be considered for the complete MB decolourization induced by SnO_p2 sample. To confirm the superior photocatalytic activity of SnO_p2, FT-IR spectra in ATR mode of this sample powder before (Figure 6F black trace) and after (Figure 6F blue trace) adsorption in dark and at end of the photocatalytic experiment (Figure 6G) have been recorded and compared to that of the MB (Figure 6E), to rule out the presence of residual MB adsorbed at the photocatalyst surface. MB FT-IR spectrum displays the framework vibration of benzene ring, the C=N stretching vibration at 1595 cm^{-1}, absorption peak of C-N at 1354 cm^{-1}, C=S stretching vibration at 1250 cm^{-1} and those at 1222 cm^{-1}, 1177 cm^{-1}, 1141 cm^{-1} assigned to the in-plane bending vibration peaks of aromatic C-H. These characteristic vibration modes of the MB, detected in the FT-IR spectrum of the SnO_p2 after adsorption, superimposed to those characteristics of the SnO_2 structure, are no longer discernible in the FT-IR spectrum of the SnO_p2 at the end of the photocatalytic experiments. The disappearance of the characteristic peaks of C=N and C=S after photocatalytic oxidation process and those of benzene ring and aromatic C-H bending vibration suggests that the N-S heterocyclic compound as well as the phenyl structure has been broken during the photocatalytic experiments,[58] and only small residual fragments can be expected still absorbed at the photocatalyst surface.

The photoactivity of each synthesized SnO_2 nanostructures has been rationalized by considering their band edge potential, estimated by VB-XPS measurements (Figure S2) combined with E_{gap} value calculated by Tauc plot (Scheme 1). In all the SnO_2 nanostructures, valence band maximum (VBM) results shifted to less positive potential, while conduction band minimum (CBM) is located at more negative potential than bulk SnO_2 (Scheme 1). A better matching between VBM potential and redox potential of $H_2O/\cdot OH$ is, hence, expected for all the samples compared to bulk SnO_2. In addition, it could not be ruled out injection of the photogenerated holes from the VBM of SnO_2 nanostructures into the HOMO of MB, bringing to direct MB oxidation.[59]

The prominent shift to higher negative value of the CBM potential in SnO_h1, due to quantum confinement, suggests photogenerated electron-induced reduction of adsorbed oxygen molecules to $\cdot O_2^-$, from which production of other ROS can be triggered, as for TiO_2 P25.

Based on the collective findings, the following hypothesis can be formulated to explain the behaviour shown by the two best performing photocatalysts, SnO_h1 and SnO_p2. The almost complete photocatalytic decolouration of MB by SnO_h1 can be mainly related to the band edge potential, better matching with the redox potentials of $H_2O/OH\cdot$ and $O_2/\cdot O_2^-$ couples, while the

superior decolouration shown by SnO_p2 is mainly driven by this photocatalyst texture, also affected by its rod-like morphology. The large adsorption capability, demonstrated for MB and expected for water molecules (or hydroxyl ions), can favour MB decolouration via direct or ·OH-mediated oxidation. In addition, the presence in this sample of the Sn_3O_4 mesophase, characterized by lower E_{gap} and surface defects can limit photogenerated electron-hole recombination, contributing to the enhancement of the photocatalytic activity.

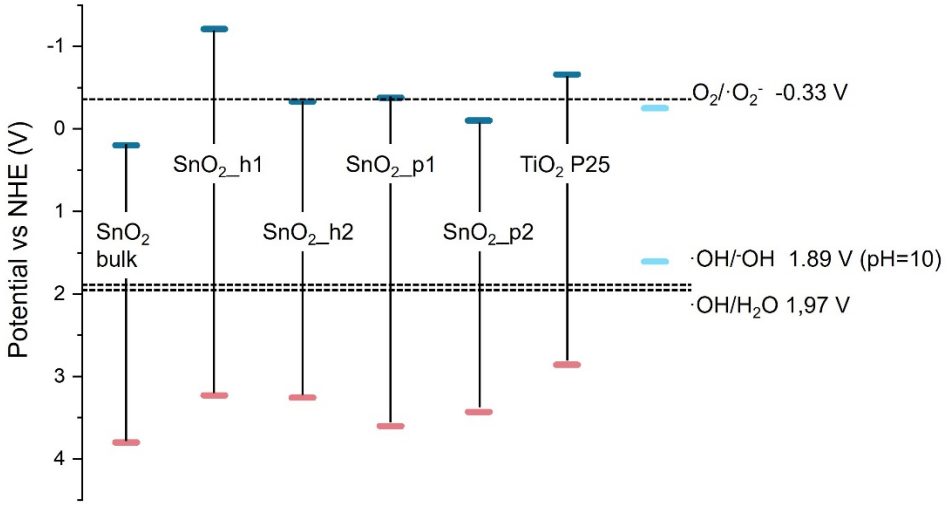

Scheme 1. Schematic representation of the electronic band-edge potential (red symbol: valence band maximum, blue symbol: conduction band minimum) of each as-prepared SnO_2 photocatalysts, as measured by Valence band (VB)-XPS and optical band gap estimated by Tauc plot, and bulk SnO_2 and TiO_2 P25 as reported in reference [44, 45] at pH=7: The Methylene Blue (MB) HOMO and LUMO potential (pale blue labels) and the redox potential of the main reactive oxygen species are also reported in Reference [47]

Even though SnO_h2 shows a texture like SnO_p2 and similar morphology and electronic properties, it has poor ·OH generation and does not feature an adsorption activity towards MB like SnO_p2. The difference in the "surface activity" can be ascribed to the presence in this sample of surface states identified as tin oxyhydroxide by FT-IR characterization, hence to a surface chemistry that unlike SnO_p2, probably hinders adsorption and induces poor ·OH generation. Therefore, the mild pH condition used for the hydrothermal synthesis of SnO_h1 proves highly effective in producing a high-performance photocatalyst. This efficacy is attributed to favorable electronic properties and surface activity, both promoting the rapid decolorization of MB. However, the most effective photocatalyst turns to be SnO_p2, synthesized via precipitation method. Its unique textural and surface properties provides superior dye adsorption capability and

the redox potential of the photogenerated holes promotes complete oxidation of the MB, in solution and adsorbed at the photocatalyst surface, via direct or ·OH-mediated reactions.

SnO_2 photocatalyst recyclability and reusability. The photocatalytic studies carried out suggest that the best candidates for short-time decolouration of MB is SnO_p2. However, for its reusability it is important to demonstrate the photocatalysts regeneration and preserved photocatalytic efficiency. FT-IR characterization of SnO_p2 at the different stage of photocatalytic experiment (adsorption under dark and UV-irradiation, Figure 6F-G) has pointed out that MB, adsorbed at the photocatalysts surface, has been completely decoloured after UV-light irradiation during the photocatalytic test. Photocatalyst reusability has been thus investigated and percentage of MB decolouration of 96%, 90% and 91% have been obtained after three successive photocatalytic cycles. Although a slight decrease in the decolourization efficiency has been observed, probably attributed to catalyst losses occurring during recovering procedures, the SnO_p2 sample confirms its effectiveness in the decolouration of MB.

4. Conclusions.

In this work we have introduced straightforward and cost-effective synthetic methods for achieving rod-like and spherical NPs by either hydrothermal or precipitation approach and propose a mechanism to explain the observed morphology modulation. Comprehensive characterization techniques, including morphological, optical, textural analysis, revealed important insight into the strong relationship between synthetic conditions and material properties, further highlighted by exploiting the synthesized materials as photocatalysts.

Strongly alkaline condition has been requested to promote rod-like nanostructures in hydrothermal methods, while shape modulation has been demonstrated to depend on the reaction mixture heating not exceeding 80°C. Regardless the synthetic procedures, spherical NPs exhibit quantum-confinement effects, while the rod-like nanostructures are characterised by the presence of an additional low-band gap Sn_3O_4 mesophase, along with near band-edge defect states, and high SSA. Moreover, strong alkaline condition in hydrothermal synthesis concomitantly induced the presence of tin oxyhydroxide surface functionalities.

The role played by the electronic band structure and surface properties, such as specific surface area, surface charge densities, and surface chemistry, in regulating the photoelectrochemical

properties of the synthesized SnO_2 nanostructures have been pinpointed by exploring the photocatalytic decolouration of MB.

Even though rod-like NPs possess a high SSA, the presence of tin oxyhydroxide surface functionalities in SnO_h2 sample has been found hindered the generation of ·OH radicals, thus limiting the photocatalytic activity. Conversely, quantum confined spherical SnO_h1, obtained under mild pH condition, despite its smaller SSA, shows surface properties and band edge potential conducive to rapid and nearly complete decolorization of MB. Conversely, the low specific surface area, small total pore volume and positive surface charge density of spherical SnO_p1 NPs, synthesized via precipitation approach, restricted their photocatalytic activity towards MB solution at nearly neutral pHs. On the other hand, rod-like SnO_p2, demonstrated to be the most efficient photocatalyst, achieving complete dye decolorization within 60 minutes. Its large SSA facilitated high MB adsorption yield, while the VBM potential promoted fast MB direct or ·OH- mediated oxidation.

These results underscore the intricate interplay between synthesis methodologies, NP structure, properties, and photoactivity. This highlights the potential for deliberate manipulation of these factors to enhance material physical-chemical properties in view of their (photo/electro)catalytic application.

Declaration

Competing interest. The authors declare that they have no known competing financial interests or personal relationships that could have appeared to influence the work reported in this paper.

Data availability.

Data will be made available on request.

CRediT authorship contribution statement. The manuscript was written through contributions of all authors. All authors have given approval to the final version of the manuscript. E. F., M. L. C. conceive the project; R. Co., M. S., G. G., C. G., M. L. C. E.F. provided the resource and fundings for project's development; A. Ma, A. P., M. L. C., E. F. supervisioned the work; M. G., M. T., R. D. F., P. L., A. M., G. V. B., T. S., R. C., M. D., C. N. D., I. D. P. E. F. carried out experimental investigation, formal analysis and validation of the results; M. G., M. T., A. M. G.

V. B., T. S. , R. C., M. S., M. L. C., E. F. wrote the original draft and G. G., C. G., C. N. D., R. Co., A. P., A. Ma., M. S., M. L. C., E. F edited the manuscript.

Acknowledgements.

This work has been supported by the Italian PRIN 2022 PNNR Project "Photocatalytically-regenerable hierarchically porous adsorbents for efficient water treatment" (Photopad cod. P2022FP2W4, 2023-2025), PON R&I ECOTEC (2014–2020 ARS01_00951), NEST - Network 4 Energy Sustainable Transition (PE2 NEST PNRR– PE0000021, 2022-2025), Hybrid ElectROchemical Energy storage in Sustainable batteries (HEROES - cod P2022AFYZX, 2023-2025), by the European Union – NextGeneration EU from the Italian Ministry of Environment and Energy Security POR H2 AdP MMES/ENEA with involvement of CNR and RSE, PNRR - Mission 2, Component 2, Investment 3.5 "Ricerca e sviluppo sull'idrogeno" CUP B93C22000630006 and by the IEMAP -Italian Energy Materials Acceleration Platform - Mission Innovation.

References

(1) Chen, L.; Liu, Z.; Guo, Z.; Huang, X.-J. Regulation of intrinsic physicochemical properties of metal oxide nanomaterials for energy conversion and environmental detection applications. *Journal of Materials Chemistry A* **2020,** *8* (34), 17326-17359, DOI: 10.1039/D0TA05539E.

(2) Concina, I.; Ibupoto, Z. H.; Vomiero, A. Semiconducting Metal Oxide Nanostructures for Water Splitting and Photovoltaics. *Advanced Energy Materials* **2017,** *7* (23), 1700706, DOI: https://doi.org/10.1002/aenm.201700706.

(3) Xiong, Y.; Lin, Y.; Wang, X.; Zhao, Y.; Tian, J. Defect engineering on SnO_2 nanomaterials for enhanced gas sensing performances. *Advanced Powder Materials* **2022,** *1* (3), 100033, DOI: https://doi.org/10.1016/j.apmate.2022.02.001.

(4) Venkateshaiah, A.; Černík, M.; Padil, V. V. T. Metal Oxide Nanoparticles for Environmental Remediation. In *Nanotechnology for Environmental Remediation*; 2022; pp 183-213.

(5) Garcia Romero, D.; Di Mario, L.; Yan, F.; Ibarra-Barreno, C. M.; Mutalik, S.; Protesescu, L.; Rudolf, P.; Loi, M. A. Understanding the Surface Chemistry of SnO_2 Nanoparticles for High Performance and Stable Organic Solar Cells. *Advanced Functional Materials* **2024,** *34* (6), 2307958, DOI: https://doi.org/10.1002/adfm.202307958.

(6) Yoon, Y.; Truong, P. L.; Lee, D.; Ko, S. H. Metal-oxide nanomaterials synthesis and applications in flexible and wearable sensors. *ACS Nanoscience Au* **2021,** *2* (2), 64-92.

(7) Sukriti; Chand, P. Effect of pH values on the structural, optical and electrical properties of SnO_2 nanostructures. *Optik* **2019,** *181*, 768-778, DOI: https://doi.org/10.1016/j.ijleo.2018.10.203.

(8) Kwon, H. J.; Shin, K.; Soh, M.; Chang, H.; Kim, J.; Lee, J.; Ko, G.; Kim, B. H.; Kim, D.; Hyeon, T. Large-Scale Synthesis and Medical Applications of Uniform-Sized Metal Oxide Nanoparticles. *Advanced Materials* **2018,** *30* (42), 1704290, DOI: https://doi.org/10.1002/adma.201704290.

(9) Sun, C.; Yang, J.; Xu, M.; Cui, Y.; Ren, W.; Zhang, J.; Zhao, H.; Liang, B. Recent intensification strategies of SnO_2-based photocatalysts: A review. *Chemical Engineering Journal* **2022,** *427*, 131564, DOI: https://doi.org/10.1016/j.cej.2021.131564.
(10) Sudapalli, A. M.; Shimpi, N. G. Tetragonal SnO_2 Nanoparticles: An Efficient Photocatalyst for the Degradation of Hazardous Ionic Dyes. *ChemistrySelect* **2023,** *8* (1), e202203310, DOI: https://doi.org/10.1002/slct.202203310.
(11) Elango, G.; Roopan, S. M. Efficacy of SnO_2 nanoparticles toward photocatalytic degradation of methylene blue dye. *Journal of Photochemistry and Photobiology B: Biology* **2016,** *155*, 34-38, DOI: https://doi.org/10.1016/j.jphotobiol.2015.12.010.
(12) Skripkin, E.; Podurets, A. A.; Kolokolov, D.; Burmistrova, A.; Bobrysheva, N.; Osmolowsky, M.; Voznesenskiy, M. A.; Osmolovskaya, O. Ultrasmall SnO_2 Nanoparticles: Influence of O-Vacancies on the Photocatalytic Degradation of Dyes. *ACS Applied Nano Materials* **2024,** *7* (6), 6093-6108, DOI: 10.1021/acsanm.3c05997.
(13) Shabna, S.; Dhas, S. S. J.; Biju, C. Potential progress in SnO_2 nanostructures for enhancing photocatalytic degradation of organic pollutants. *Catalysis Communications* **2023**, 106642.
(14) Hu, P.; Liang, G.; Zhu, B.; Macyk, W.; Yu, J.; Xu, F. Highly Selective Photoconversion of CO_2 to CH_4 over SnO_2/$Cs_3Bi_2Br_9$ Heterojunctions Assisted by S-Scheme Charge Separation. *ACS Catalysis* **2023,** *13* (19), 12623-12633, DOI: 10.1021/acscatal.3c03095.
(15) Shang, Y.; Liu, T.; Chen, G.; Alborzi, E.; Yong, X.; Wang, Y. N,P co-doped carbon quantum dots bridge g-C_3N_4 and SnO_2: Accelerating charge transport in S-scheme heterojunction for enhanced photocatalytic hydrogen production. *Journal of Alloys and Compounds* **2024,** *971*, 172667, DOI: https://doi.org/10.1016/j.jallcom.2023.172667.
(16) Zafar, Z.; Yi, S.; Li, J.; Li, C.; Zhu, Y.; Zada, A.; Yao, W.; Liu, Z.; Yue, X. Recent Development in Defects Engineered Photocatalysts: An Overview of the Experimental and Theoretical Strategies. *ENERGY & ENVIRONMENTAL MATERIALS* **2022,** *5* (1), 68-114, DOI: https://doi.org/10.1002/eem2.12171.
(17) Michalec, K.; Kusior, A. From Adsorbent to Photocatalyst: The Sensitization Effect of SnO_2 Surface towards Dye Photodecomposition. *Molecules* **2021,** *26* (23), 7123.
(18) Li, M.; Ma, L.; Luo, L.; Liu, Y.; Xu, M.; Zhou, H.; Wang, Y.; Li, Z.; Kong, X.; Duan, H. Efficient photocatalytic epoxidation of styrene over a quantum-sized SnO_2 on carbon nitride as a heterostructured catalyst. *Applied Catalysis B: Environmental* **2022,** *309*, 121268, DOI: https://doi.org/10.1016/j.apcatb.2022.121268.
(19) Ayyub, M. M.; Rao, C. N. R. 1 - Design of efficient photocatalysts through band gap engineering. In *Nanostructured Photocatalysts*; Boukherroub, R.; Ogale, S. B.; Robertson, N., Eds.; Elsevier: 2020; pp 1-18.
(20) Huo, Y.; Zhang, P.; Chi, J.; Fang, F.; Song, Y.; Sun, D. Surface Functionalization and Defect Construction of SnO_2 with Amine Group for Enhanced Visible-Light-Driven Photocatalytic CO_2 Reduction. *Advanced Energy Materials n/a* (n/a), 2304282, DOI: https://doi.org/10.1002/aenm.202304282.
(21) Raizada, P.; Soni, V.; Kumar, A.; Singh, P.; Parwaz Khan, A. A.; Asiri, A. M.; Thakur, V. K.; Nguyen, V.-H. Surface defect engineering of metal oxides photocatalyst for energy application and water treatment. *Journal of Materiomics* **2021,** *7* (2), 388-418, DOI: https://doi.org/10.1016/j.jmat.2020.10.009.
(22) Zhang, Y.; Li, L.; Zheng, J.; Li, Q.; Zuo, Y.; Yang, E.; Li, G. Two-Step Grain-Growth Kinetics of Sub-7 nm SnO_2 Nanocrystal under Hydrothermal Condition. *The Journal of Physical Chemistry C* **2015,** *119* (33), 19505-19512, DOI: 10.1021/acs.jpcc.5b05282.

(23) Dong, Q.; Shi, Y.; Zhang, C.; Wu, Y.; Wang, L. Energetically favored formation of SnO_2 nanocrystals as electron transfer layer in perovskite solar cells with high efficiency exceeding 19%. *Nano Energy* **2017,** *40*, 336-344, DOI: https://doi.org/10.1016/j.nanoen.2017.08.041.
(24) Bouaine, A.; Brihi, N.; Schmerber, G.; Ulhaq-Bouillet, C.; Colis, S.; Dinia, A. Structural, Optical, and Magnetic Properties of Co-doped SnO_2 Powders Synthesized by the Coprecipitation Technique. *The Journal of Physical Chemistry C* **2007,** *111* (7), 2924-2928, DOI: 10.1021/jp066897p.
(25) Chen, C.; Jiang, Y.; Guo, J.; Wu, X.; Zhang, W.; Wu, S.; Gao, X.; Hu, X.; Wang, Q.; Zhou, G.; Chen, Y.; Liu, J.-M.; Kempa, K.; Gao, J. Solvent-Assisted Low-Temperature Crystallization of SnO_2 Electron-Transfer Layer for High-Efficiency Planar Perovskite Solar Cells. *Advanced Functional Materials* **2019,** *29* (30), 1900557, DOI: https://doi.org/10.1002/adfm.201900557.
(26) Zhu, Z.; Bai, Y.; Liu, X.; Chueh, C.-C.; Yang, S.; Jen, A. K.-Y. Enhanced Efficiency and Stability of Inverted Perovskite Solar Cells Using Highly Crystalline SnO_2 Nanocrystals as the Robust Electron-Transporting Layer. *Advanced Materials* **2016,** *28* (30), 6478-6484, DOI: https://doi.org/10.1002/adma.201600619.
(27) Sato, K.; Yokoyama, Y.; Valmalette, J.-C.; Kuruma, K.; Abe, H.; Takarada, T. Hydrothermal Growth of Tailored SnO_2 Nanocrystals. *Crystal Growth & Design* **2013,** *13* (4), 1685-1693, DOI: 10.1021/cg400013q.
(28) Ghosh, S.; Das, K.; Chakrabarti, K.; De, S. K. Effect of oleic acid ligand on photophysical, photoconductive and magnetic properties of monodisperse SnO_2 quantum dots. *Dalton Transactions* **2013,** *42* (10), 3434-3446, DOI: 10.1039/C2DT31764H.
(29) Asdim; Manseki, K.; Sugiura, T.; Yoshida, T. Microwave synthesis of size-controllable SnO_2 nanocrystals for dye-sensitized solar cells. *New Journal of Chemistry* **2014,** *38* (2), 598-603, DOI: 10.1039/C3NJ01278F.
(30) Cho, I.; Kang, K.; Yang, D.; Yun, J.; Park, I. Localized Liquid-Phase Synthesis of Porous SnO_2 Nanotubes on MEMS Platform for Low-Power, High Performance Gas Sensors. *ACS Applied Materials & Interfaces* **2017,** *9* (32), 27111-27119, DOI: 10.1021/acsami.7b04850.
(31) Yang, L.; Huang, J.; Shi, L.; Cao, L.; Liu, H.; Liu, Y.; Li, Y.; Song, H.; Jie, Y.; Ye, J. Sb doped SnO_2-decorated porous g-C_3N_4 nanosheet heterostructures with enhanced photocatalytic activities under visible light irradiation. *Applied Catalysis B: Environmental* **2018,** *221*, 670-680, DOI: https://doi.org/10.1016/j.apcatb.2017.09.041.
(32) Jose, L. M.; George, N. S.; Kadam, S. A.; Athira, S.; A, K.; Aravind, A.; Ma, Y.-R.; Chen, Y.-R. Insight into the adsorption, photocatalytic and magnetic properties of bandgap tailored hydrothermally grown SnO_2:Ni/Cu nanostructures. *Optical Materials* **2023,** *135*, 113348, DOI: https://doi.org/10.1016/j.optmat.2022.113348.
(33) Kandathil, V.; Manoj, N. Advances in CO_2 utilization employing anisotropic nanomaterials as catalysts: a review. *Frontiers in Chemistry* **2023,** *11*, DOI: 10.3389/fchem.2023.1175132.
(34) Birkel, A.; Loges, N.; Mugnaioli, E.; Branscheid, R.; Koll, D.; Frank, S.; Panthöfer, M.; Tremel, W. Interaction of Alkaline Metal Cations with Oxidic Surfaces: Effect on the Morphology of SnO_2 Nanoparticles. *Langmuir* **2010,** *26* (5), 3590-3595, DOI: 10.1021/la902994r.
(35) Karmaoui, M.; Jorge, A. B.; McMillan, P. F.; Aliev, A. E.; Pullar, R. C.; Labrincha, J. A.; Tobaldi, D. M. One-Step Synthesis, Structure, and Band Gap Properties of SnO_2 Nanoparticles Made by a Low Temperature Nonaqueous Sol–Gel Technique. *ACS Omega* **2018,** *3* (10), 13227-13238, DOI: 10.1021/acsomega.8b02122.
(36) Ahmad, T.; Ansari, M. Z. Structural and optical characteristics of Sb doped SnO_2 nanoparticles and their boosted photocatalytic activity under visible light irradiation. *Ceramics*

International **2023,** *49* (22, Part B), 35740-35756, DOI: https://doi.org/10.1016/j.ceramint.2023.08.253.
(37) Kar, A.; Kundu, S.; Patra, A. Surface Defect-Related Luminescence Properties of SnO_2 Nanorods and Nanoparticles. *The Journal of Physical Chemistry C* **2011,** *115* (1), 118-124, DOI: 10.1021/jp110313b.
(38) Yu, L.; Cai, D.; Wang, H.; Titirici, M.-M. Hydrothermal synthesis of SnO_2 and SnO_2@C nanorods and their application as anode materials in lithium-ion batteries. *RSC Advances* **2013,** *3* (38), 17281-17286, DOI: 10.1039/C3RA42900H.
(39) Sahu, B. K.; Das, A.; Prasad, A. K.; Mangamma, G. The Role of In-Plane Oxygen Vacancy Defects in SnO_2 Nanoparticles for CH_4 Sensing. *Journal of Nanoscience and Nanotechnology* **2019,** *19* (12), 7764-7770, DOI: 10.1166/jnn.2019.16736.
(40) Gole, J. L.; Iretskii, A. V.; White, M. G.; Jacob, A.; Carter, W. B.; Prokes, S. M.; Erickson, A. S. Suggested Oxidation State Dependence for the Activity of Submicron Structures Prepared from Tin/Tin Oxide Mixtures. *Chemistry of Materials* **2004,** *16* (25), 5473-5481, DOI: 10.1021/cm030618i.
(41) Liu, Y.-K.; Dong, Y.; Wang, G.-H. Low-Frequency and Abnormal Raman Spectrum in SnO_2 Nanorods. *Chinese Physics Letters* **2004,** *21* (1), 156, DOI: 10.1088/0256-307X/21/1/047.
(42) Nikiforov, A.; Timofeev, V.; Mashanov, V.; Azarov, I.; Loshkarev, I.; Volodin, V.; Gulyaev, D.; Chetyrin, I.; Korolkov, I. Formation of SnO and SnO2 phases during the annealing of $SnO_{(x)}$ films obtained by molecular beam epitaxy. *Applied Surface Science* **2020,** *512*, 145735.
(43) Velmurugan, G.; Ganapathi Raman, R.; Prakash, D.; Kim, I.; Sahadevan, J.; Sivaprakash, P. Influence of Ni and Sn Perovskite $NiSn(OH)_6$ Nanoparticles on Energy Storage Applications. *Nanomaterials* **2023,** *13* (9), 1523.
(44) Mills, A. An overview of the methylene blue ISO test for assessing the activities of photocatalytic films. *Applied Catalysis B: Environmental* **2012,** *128*, 144-149, DOI: https://doi.org/10.1016/j.apcatb.2012.01.019.
(45) Wu, L.; Xie, Q.; Lv, Y.; Wu, Z.; Liang, X.; Lu, M.; Nie, Y. Degradation of Methylene Blue via Dielectric Barrier Discharge Plasma Treatment. *Water* **2019,** *11* (9), 1818.
(46) Houas, A.; Lachheb, H.; Ksibi, M.; Elaloui, E.; Guillard, C.; Herrmann, J.-M. Photocatalytic degradation pathway of methylene blue in water. *Applied Catalysis B: Environmental* **2001,** *31* (2), 145-157, DOI: https://doi.org/10.1016/S0926-3373(00)00276-9.
(47) Ayu, D. G.; Gea, S.; Andriayani; Telaumbanua, D. J.; Piliang, A. F. R.; Harahap, M.; Yen, Z.; Goei, R.; Tok, A. I. Y. Photocatalytic Degradation of Methylene Blue Using N-Doped ZnO/Carbon Dot (N-ZnO/CD) Nanocomposites Derived from Organic Soybean. *ACS Omega* **2023,** *8* (17), 14965-14984, DOI: 10.1021/acsomega.2c07546.
(48) Khan, I.; Saeed, K.; Zekker, I.; Zhang, B.; Hendi, A. H.; Ahmad, A.; Ahmad, S.; Zada, N.; Ahmad, H.; Shah, L. A.; Shah, T.; Khan, I. Review on Methylene Blue: Its Properties, Uses, Toxicity and Photodegradation. *Water* **2022,** *14* (2), 242.
(49) Fernández-Pérez, A.; Marbán, G. Visible Light Spectroscopic Analysis of Methylene Blue in Water; What Comes after Dimer? *ACS Omega* **2020,** *5* (46), 29801-29815, DOI: 10.1021/acsomega.0c03830.
(50) Kosmulski, M. pH-dependent surface charging and points of zero charge II. Update. *Journal of Colloid and Interface Science* **2004,** *275* (1), 214-224, DOI: https://doi.org/10.1016/j.jcis.2004.02.029.
(51) Moreau, F.; Bond, G. C. Preparation and reactivation of Au/TiO_2 catalysts. *Catalysis Today* **2007,** *122* (3), 260-265, DOI: https://doi.org/10.1016/j.cattod.2007.01.017.

(52) Hidaka, H.; Zhao, J.; Pelizzetti, E.; Serpone, N. Photodegradation of surfactants. 8. Comparison of photocatalytic processes between anionic DBS and cationic BDDAC on the titania surface. *The Journal of Physical Chemistry* **1992,** *96* (5), 2226-2230, DOI: 10.1021/j100184a037.
(53) Li, J.; Ma, W.; Chen, C.; Zhao, J.; Zhu, H.; Gao, X. Photodegradation of dye pollutants on one-dimensional TiO_2 nanoparticles under UV and visible irradiation. *Journal of Molecular Catalysis A: Chemical* **2007,** *261* (1), 131-138, DOI: https://doi.org/10.1016/j.molcata.2006.08.018.
(54) Kar, A.; Olszówka, J.; Sain, S.; Sloman, S.-R. I.; Montes, O.; Fernández, A.; Pradhan, S. K.; Wheatley, A. E. H. Morphological effects on the photocatalytic properties of SnO_2 nanostructures. *Journal of Alloys and Compounds* **2019,** *810*, 151718, DOI: https://doi.org/10.1016/j.jallcom.2019.151718.
(55) Velo-Gala, I.; Torres-Pinto, A.; Silva, C. G.; Ohtani, B.; Silva, A. M. T.; Faria, J. L. Graphitic carbon nitride photocatalysis: the hydroperoxyl radical role revealed by kinetic modelling. *Catalysis Science & Technology* **2021,** *11* (23), 7712-7726, DOI: 10.1039/D1CY01657A.
(56) Wang, L.; Zhang, Q.; Chen, B.; Bu, Y.; Chen, Y.; Ma, J.; Rosario-Ortiz, F. L.; Zhu, R. Some issues limiting photo(cata)lysis application in water pollutant control: A critical review from chemistry perspectives. *Water Research* **2020,** *174*, 115605, DOI: https://doi.org/10.1016/j.watres.2020.115605.
(57) Dai, S.; Yao, Z. Synthesis of flower-like SnO_2 single crystals and its enhanced photocatalytic activity. *Applied Surface Science* **2012,** *258* (15), 5703-5706, DOI: https://doi.org/10.1016/j.apsusc.2012.02.065.
(58) Wang, X.-q.; Han, S.-f.; Zhang, Q.-w.; Zhang, N.; Zhao, D.-d. Photocatalytic oxidation degradation mechanism study of methylene blue dye waste water with GR/iTO_2. *MATEC Web Conf.* **2018,** *238*, 03006.
(59) Li, Q.; Li, X.; Wageh, S.; Al-Ghamdi, A. A.; Yu, J. CdS/Graphene Nanocomposite Photocatalysts. *Advanced Energy Materials* **2015,** *5* (14), 1500010, DOI: https://doi.org/10.1002/aenm.201500010.